Functional Materials Letters
1950087 (5 pages)
© World Scientific Publishing Company
DOI: 10.1142/S1793604719500875

World Scientific
www.worldscientific.com

Funct. Mater. Lett. Downloaded from www.worldscientific.com
by UNIVERSITY OF NEW ENGLAND on 09/21/19. Re-use and distribution is strictly not permitted, except for Open Access articles.

Reducing parasitic absorption and recombination losses in silicon solar cells through transition metal doped glass frit

Xing Jiang, Zhou Gao, Xingbo Wang, Yongji Chen, Jian Liu, Mingjian Zhang,
Yuan Lin and Feng Pan*
School of Advanced Materials
Peking University Shenzhen Graduate School
Shenzhen 518055, P. R. China
**panfeng@pkusz.edu.cn*

Received 2 June 2019; Accepted 9 July 2019; Published 26 August 2019

Efficient electron selective contacts, smoother rear silicon surface and passivation of silicon-electrode interfaces could reduce parasitic light absorption and electron-hole recombination. Therefore, they are necessary for high conversion efficiency in silicon solar cells. In this work, a novel transition metal doped glass frit is fabricated and introduced into pristine Al paste. As a result, the average power conversion efficiency (PCE) of cells is improved from 17.9 to 18.3%. Combining several results, the improvement can be attributed to three key factors: (a) a thicker back surface field (BSF) layer that blocks electrons; (b) a smoother rear silicon surface which leads to less parasitic absorption; and (c) glass frit coating on aluminum particles which may facilite hole-transfer from silicon layer to aluminum electrode.

Keywords: Al paste; glass; BSF; parasitic absorption; recombination.

Parasitic absorption and electronic recombination losses have been an obvious barrier in the way to silicon solar cells' theoretical maximum efficiency.[1] In previous researches, there are two common ways to reduce parasitic absorption and electron-hole recombination losses.

The first one is developing new cell structures.[2–6] Passivated emitter and rear cell (PERC) is one of the most representative new structures and has occupied a large share in photovoltaic market due to the enhanced conversion efficiency. But it also leads to a higher cost of manufacturing for its complex cell structure and requirement of harsh production environment such as high vacuum.[2]

The other way is introducing an electron-selective layer between silicon layer and electrodes. Electron-selective layers, sometimes called electron selective contacts or hole-transport layer, can transmit holes and blocks electrons.[7] Inorganic *p*-type metal oxides have been widely used as electron-selective materials for thin-film solar cells due to their high work function, chemical stability and low cost.[8–14] There have been several reports about employing transition metal oxide as electron selective layer in silicon solar cells.[7,15–20] In these works, production of oxide layer needed special technologies, such as thermal evaporation, atomic layer deposition (ALD) or plasma-enhanced chemical vapor deposition (PECVD), which also bring a large cost. Tong *et al.* reported that spin-coating film showed comparable contact resistivity and passivation quality on c-Si wafers with thermally evaporated film, demonstrating its potential to be an effective electron selective layer for c-Si solar cells and an alternative for thermally evaporated films.[13] But Lu *et al.* prepared this film by solution-based synthesis method on c-Si cells and only gained a PCE of 7.26%.[21] This result shows the limitation of spin-coating film in practical application.

As shown in Fig. 1(a), conventional crystalline silicon cells can be separated into four parts including front electrode (usually Ag paste), anti-reflection layer (usually SiN_x), silicon layer (*p*-type and *n*-type silicon) and back electrode (usually Al paste). Cross-sectional scanning electron microscope (SEM) image (Fig. 1(b)) reveals more details such as back surface of device being composed of silicon layer, black surface field (BSF), Al-Si solid layer and aluminum layer.[22] In this paper, we successfully fabricated a novel transition metal doped glass frit (see in supporting information) and demonstrated that Al paste with this glass frit can effectively enhance PCE of crystalline silicon solar cells. We adjusted the mass fraction of glass in pristine Al paste and gained the highest PCE of 18.3% when 0.5 wt.% of glass was mixed in pristine Al paste (Figs. S1(a)–S1(d)). Photovoltaic performance

*Corresponding author.

Funct. Mater. Lett. Downloaded from www.worldscientific.com
by UNIVERSITY OF NEW ENGLAND on 09/21/19. Re-use and distribution is strictly not permitted, except for Open Access articles.

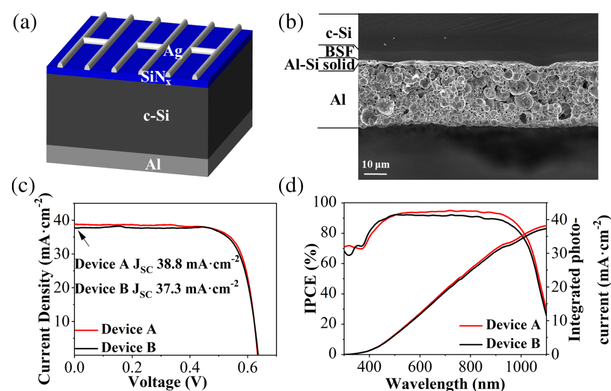

Fig. 1. (a) Schematic illustration of device structure (Ag/SiN_x/c-Si/Al paste). (b) Cross-sectional SEM image of device. Rear structure of the cell includes c-Si/BSF/Al-Si solid/Al particles. J–V curves. (c) and EQE images. (d) for champions of Device A and Device B.

of Device A (with 0.5 wt.% glass in Al paste) and Device B (pristine Al paste) demonstrates the advantage of Device A especially on short circuit current density (J_{SC}) parameter. Figure 1(c) shows curves of the current density-voltage (J–V) characteristics for champions of Devices A and B. As a result, champion of Device A exhibits a higher J_{SC} of 38.8 mA · cm^{-2} than Device B of 37.3 mA · cm^{-2}. These cells behave similar on other parameters, including open-circuit voltage (V_{OC}) of 634 (Device A) and 637 mV (Device B), fill factor (FF) of 0.770 (Device A) and 0.774 (Device B). As a result, champion of Device A shows better PCE of 18.9% than Device B of 18.4%. Table 1 summarizes photovoltaic parameters of a batch of devices (13 for Device A and 18 for Device B). Average values of photovoltaic parameters show the same trend as the best ones. External quantum efficiency (EQE) measurement helps explain the improvement of J_{SC} (Fig. 1(d)). The integrated J_{SC} of Device A is 38.2 mA · cm^{-2} and of Device B is 37.3 mA · cm^{-2}, according to the photovoltaic parameters. Device A with glass can converse more photons to electrons especially when wavelength of incident light turns to long wave. Battaglia *et al.*[7,23] reported similar result when inserting transition metal oxide layer between the oxide contact and silicon layer. In this way, they gained a dramatic increase in blue and visible response together with a 1.9 mA · cm^{-2} gain in photocurrent compared with standard cells without transition metal oxide layer. In their work, transition metal oxide is

Table 1. Summary of photovoltaic parameters for Device A (13 cells) and Device B (18 cells).

Al paste		J_{SC} (mA · cm^{-2})	V_{OC} (mV)	FF	PCE (%)
Device A	best	38.8	634	0.770	18.9
	mean ± SD	38.2 ± 0.3	634 ± 2	0.756 ± 0.011	18.3 ± 0.3
Device B	best	37.3	637	0.774	18.4
	mean ± SD	37.4 ± 0.3	637 ± 3	0.751 ± 0.010	17.9 ± 0.3

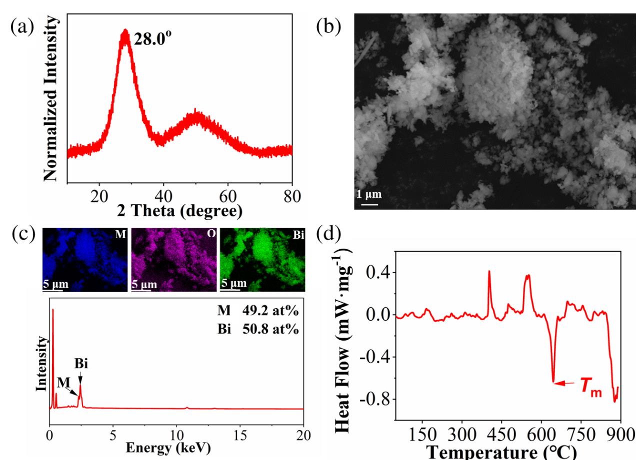

Fig. 2. (a) XRD patterns of the glass frit, (b) SEM image shows scale of glass frit is micron, (c) EDS result of glass together with elementary mapping, atom percent of the transition metal oxide and Bi, (d) DSC curve of glass frit in nitrogen from 25°C to 650°C with a heating rate of 10 K · min^{-1}.

considered to act as a high work function metal with a low density of states at the Fermi level. With a large bandgap of 3.3 eV, transition metal oxide contacts can reduce parasitic absorption of light and gain a larger J_{SC} while maintaining the same V_{OC}. This can help explain our result of increasement on J_{SC}. Furthermore, according to the work of Rajkanan *et al.*, the absorption coefficient of silicon decreases rapidly with the increase of wave length.[24] Since the absorption coefficient is low and red light can pass a reasonable distance into silicon, enhancement of long wavelength conversion efficiency can be partly attributed to reduction of recombination near rear surface of cell. Besides, Device A maintains the same V_{OC} as Device B, implying that reduction of parasitic absorption is more important than reduction of recombination.

In order to reveal other reasons for the performance improvement of Device A, properties of the glass frit were comprehensively characterized. Figure 2(a) is X-ray diffraction (XRD) pattern of the powder, which is determined as glass rather than crystal because it does not have obvious crystal peaks. This result is similar to earlier reported results.[25] Morphology of the glass is micrometer scale powders (Fig. 2(b)). Corresponding energy dispersive spectrometer (EDS) images reveal that glass is composited by B, Bi and the transition metal oxide(M), and molar ratio of the transition metal oxide and Bi accords with that in raw materials (Fig. 2(c)). XPS is used to identify the charge valence of transition metal in glass as shown in Fig. S2(a). Peaks of transition metal oxide perfect accord with reported paper,[26] but after forming into glass, oxidation state of transition metal turned from +6 to +5.[27] Differential scanning calorimetry (DSC) results in nitrogen (Fig. 2(d)) show that melt temperature (T_m) of glass frit is around 645°C. Because of its low T_m, this glass frit will soften quickly and

Funct. Mater. Lett. Downloaded from www.worldscientific.com
by UNIVERSITY OF NEW ENGLAND on 09/21/19. Re-use and distribution is strictly not permitted, except for Open Access articles.

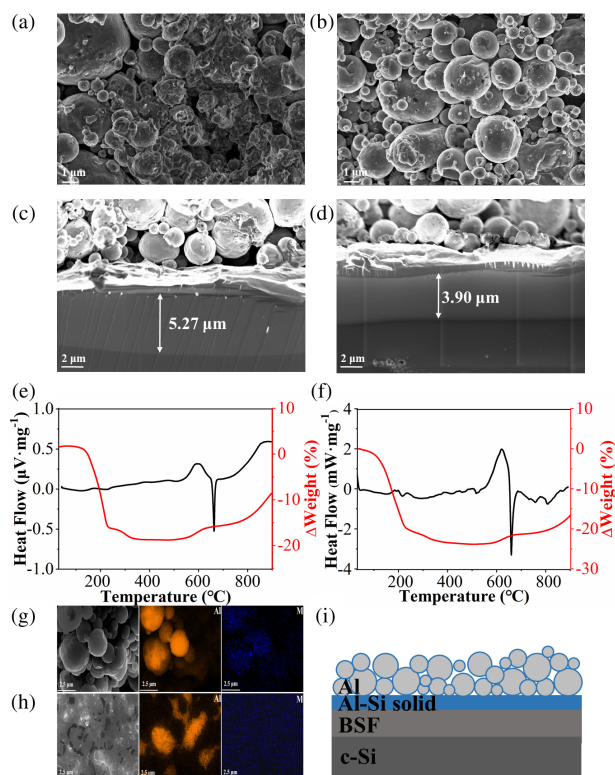

Fig. 3. (a–b) SEM images of aluminum particles of Devices A and B after firing. Aluminum particles melted greatly in Device A, even small particles melted. (c–d) Thickness of BSF layer for champions of Device A (5.27 μm for average value of three random positions) and Device B (3.90 μm for average value of three random positions). TGA/DSC curves of Al paste with 0.5 wt.% of glass (e) and pristine Al paste (f) in air from 25 to 900°C with a heating rate of $10\,K \cdot min^{-1}$. (g) Cross-sectional SEM and EDS images of Device A, glass frit coats on surface of aluminium particles uniformly after firing. (h) SEM and EDS images of Al-Si solid layer of Device A after treating in 60°C ultrasound cleaner for 2 h to remove aluminium particles. (i) Illustration of rear side structure of Device A. After firing, glass (paint with blue) will distribute among aluminium particles and surface of Al-Si solid layer.

flow when sintered in furnace with a peak temperature of 795°C.

SEM together with EDS was used to analyze the differences of device structures after introducing glass. Figures 3(a)–3(b) are cross-sectional SEM images of aluminum particles for Devices A and B. Aluminum particles of Device A melt dramatically and improve adhesion performance of Al paste. When treated in 60°C ultrasound cleaner, aluminum particles of Device A were harder to remove than Device B. A thicker BSF layer of 5.27 μm is observed in Device A (Figs. 3(c)–3(d)). Huster *et al.* provided insights about the BSF formation process in silicon cells.[22] After aluminum particles melting with a high firing temperature, more and more silicon were dissolved in the liquid phase. Then, during the cooling process, silicon together with trace aluminum is recrystallized from melt, building up the BSF layer.

Remaining liquid phase got solidified and became Al-Si solid layer. Longer time and higher firing temperature could increase the thickness.[28] However, it would lead to uneven distribution of BSF layer due to the aggravating agglomeration of Al/Si islands. So, appropriate firing temperature and time are necessary. Al_2O_3 shells on surface of aluminum particles could prevent aluminum particles to collapse during the firing process and would lead to a thinner BSF layer. Transition metal oxide can react with aluminum under a high temperature, which is widely known as thermite reaction.[29] This reaction occurs between 800 and 900 K, and will occur at a higher temperature with the increase of heating rate. TGA/DSC tests of Al pastes demonstrated that this glass with the transition metal oxide can react with aluminum (Figs. 3(e)–3(f)). TGA curve of Al paste with glass increases rapidly around 750°C together with an exothermic process according to DSC curve. The same phenomenon does not appear in pristine Al paste. This temperature of thermite reaction is similar to that of the transition metal oxide around 818°C (Fig. S3). As a result, more aluminum liquids will form and dissolve more silicons, then become a thicker BSF during the cooling process. But if excess of transition metal doped glass is added, then cells will bend seriously together with a lot of Al/Si islands on rear side after firing. As a result, PCE of cells will decrease when more than 0.5 wt.% of glass is used (Fig. S1(a)). BSF layer plays an important role in reducing electron-hole recombination. Interfaces between metal and semiconductor are regions of high recombination velocity and BSF is used to create a low recombination velocity interface and improve the probability of collection of carriers generated near the back surface. The model calculations[30] indicate that to obtain back surface recombination velocity smaller than $200\,cm \cdot s^{-1}$, the minimum BSF thickness of 6 μm is required for cells with a front doping of 75 Ω/sq. And for thickness of larger than 6 μm, back surface recombination velocity does not gain significant improvement as the thickness of BSF increases. According to this result, a thicker BSF of 5.27 μm in Device A can help improve the short circuit current of devices.[31–33] EDS images show that the shape of the transition metal signals is similar to that of aluminum (Fig. 3(g)) and we can find signals of the transition metal and Bi on the surface of Al-Si solid layer as well (Fig. 3(h)). Furthermore, XPS signals of metal on the surface of Al-Si solid layer of Device A showed same oxidation state with metal in glass. These signals will disappear after etching for 5 min by Ar^+ sputtering (Figs. S2(b)–S2(d)). We can conclude that glass frit that is introduced to Al paste will finally coat on surface of aluminum particles and Al-Si layer uniformly after firing. Figure 3(i) shows the new structure of cell with glass-containing Al paste.

Figures S4(a)–S4(d) are the SEM and EDS images of silicon on rear surface of Al-removed cells. Only signals of silicon can be found in EDS result which show that Al is completely removed. Atomic force microscopy (AFM) results (Figs. S4(e)–S4(f)) reveal that roughness of rear

Funct. Mater. Lett. Downloaded from www.worldscientific.com
by UNIVERSITY OF NEW ENGLAND on 09/21/19. Re-use and distribution is strictly not permitted, except for Open Access articles.

silicon surface of Device A is smaller than Device B. Arithmetical mean deviation of the profile (R_a) of Device A is 1.90 nm compared with Device B of 10.2 nm. It has been reported by several works[34–36] that with a decrease of silicon surface roughness, the short circuit current density will increase. Optical simulations with different models[35] prove that larger mean scatter angles come with a smoother rear surface, and lead to a less parasitical absorption. In this way, EQE of Device A can behave better than Device B on long waves for reducing parasitical absorption. This result accords with our EQE result. Reduction of silicon roughness may be caused by more silicon dissolved in aluminum liquid during the firing process. Thus, irregular structures of silicon may disappear and cause a lower roughness of silicon surface.

Change of energy band structure may be another reason for improvement on J_{SC}. Work function of Al-Si solid layer increased from 4.68 eV (Device B) to 4.81 eV (Device A) according to ultraviolet photoelectron spectroscopy (UPS) results Fig. S5(a). Increase of work function is not only detected on surface of Al-Si solid, but also on aluminum layer. UPS tests on back surface of cells show aluminum layer of Device A has a higher work function of 4.65 eV compared to Device B of 4.34 eV Fig. S5(b). Since the transition metal oxide in glass has a high work function,[7] we may ascribe tuned work function of Al-Si solid layer and Al layer to dispersed glass film. Figure S5(c) shows illustration of energy band structure on interface of Al-Si solid and *p*-type silicon. Work functions of silver and energy levels of *p*-type silicon can be referred in the published works.[37–40] Work function of Al-Si solid is smaller than *p*-type silicon, so electrons will transfer from Al-Si solid to silicon. As a result, surface of *p*-type silicon will carry negative charges and different concentrations of negative charges in silicon layer will form electric field points to internal silicon. As a result, energy band of silicon will bend. Holes need to overcome an energy barrier in order to transport from silicon to Al-Si solid. The height of the barrier depends on the difference of work function of Al-Si solid and *p*-type silicon. As discussed in Battaglia's work,[7] hole extraction efficiency may effectively improve with a higher work function of Al-Si solid and may lead to a higher J_{SC}.[14,41]

In summary, to obtain a higher J_{SC} of silicon solar cell, we suggest the feasibility of introducing high work function, large bandgap and thermite reaction possible materials to glass of Al paste. During the firing process, glass frit can help small aluminum particles melt, forming a more liquid-like phase. In this way, a thicker BSF will be formed, which reduces carrier recombination. A smoother rear silicon surface may also be resulted during the firing process. This surface can gain larger mean scatter angles of light and reduce parasitical absorption. Furthermore, glass frit will disperse on surface and interface of Al layer and tune work functions of Al-Si solid layer. In this way, glass may facilitate hole-transfer from silicon to aluminum electrode. As a result, Al paste with transition metal oxide doped glass exhibits improved J_{SC} of $0.8\,\mathrm{mA \cdot cm^{-2}}$.

Acknowledgments

This work was supported by the Soft Science Research Project of Guangdong Province (No. 2017B030301013), the Guangdong Innovative Team Program (No. 2013N080) and the Shenzhen Science and Technology Research (Grant No. JSGG20170414163208757).

References

1. W. Shockley and H. J. Queisser, *J. Appl. Phys.* **3**, 32 (1961).
2. A. W. Blakers *et al.*, *Appl. Phys. Lett.* **13**, 55 (1989).
3. J. Zhao *et al.*, *Prog. Photovolt: Res. Appl.* **3**, 2 (1994).
4. J. Zhao *et al.*, *Prog. Photovolt: Res. Appl.* **6**, 7 (1999).
5. A. W. Blakers and M. A. Green, *Appl. Phys. Lett.* **3**, 48 (1986).
6. M. A. Green, *Prog. Photovolt: Res. Appl.* **3**, 17 (2009).
7. C. Battaglia *et al.*, *Appl. Phys. Lett.* **11**, 104 (2014).
8. J. Meyer *et al.*, *Adv. Mater.* **1**, 23 (2011).
9. H. S. Kim and N. G. Park, *J. Phys. Chem. Lett.* **17**, 5 (2014).
10. J. H. Kim *et al.*, *Adv. Mater.* **4**, 27 (2015).
11. H. Peng *et al.*, *Nano Res.* **10**, 9 (2016).
12. W. Sun *et al.*, *Nanoscale* **20**, 8 (2016).
13. J. Tong *et al.*, *Appl. Surf. Sci.* **11**, 423 (2017).
14. W. Yan *et al.*, *Adv. Energy Mater.* **17**, 6 (2016).
15. J. Schmidt *et al.*, *Prog. Photovolt: Res. Appl.* **6**, 16 (2008).
16. B. Hoex *et al.*, *J. Appl. Phys.* **4**, 104 (2008).
17. S. Gatz *et al.*, *Phys. Status Solidi RRL* **4**, 5 (2011).
18. G. Dingemans and W. M. M. Kessels, *J. Vac. Sci. Technol., A* **4**, 30 (2012).
19. J. Geissbühler *et al.*, *Appl. Phys. Lett.* **8**, 107 (2015).
20. L. G. Gerling *et al.*, *Sol. Energy Mater. Sol. Cells* **145**, 109 (2016).
21. C. Lu *et al.*, Aqueous solution deposited molybdenum oxide crystalline silicon heterojunction solar cells. *2018 IEEE 7th World Conf. Photovoltaic Energy Conversion* (2018), pp. 2155–2157.
22. F. Huster, Investigation of the alloying process of screen printed aluminum pastes for the BSF formation on silicon solar cells. *Proc. 20th European Photovoltaic Solar Energy Conf.* (2005), pp. 1466–1469.
23. C. Battaglia *et al.*, *Nano Lett.* **2**, 14 (2014).
24. K. Rajkanan *et al.*, *Solid-State Electron.* **9**, 22 (1979).
25. R. Iordanova *et al.*, *J. Non-Cryst. Solids* **14**, 357 (2011).
26. L. Benoist *et al.*, *Surf. Interface Anal.* **1**, 22 (1994).
27. M. Anwar *et al.*, *J. Mater. Sci.* **9**, 24 (1989).
28. A. Kaminski *et al.*, *Sol. Energy Mater. Sol. Cells* **1**, 72 (2002).
29. S. M. Umbrajkar *et al.*, *J. Propul. Power* **2**, 24 (2008).
30. N. Chen. University of North Carolina at Charlotte, PhD dissertation (2015).
31. J. G. Fossum, *IEEE Trans. Electron Devices* **4**, 24 (1977).
32. A. Kaminski *et al.*, *Sol. Energy Mater. Sol. Cells* **1**, 72 (2002).
33. J. Zhou *et al.*, *Mater. Lett.* **169**, 197 (2016).

34. C. Schwab *et al.*, *Energy Procedia*, **27**, 522 (2012).
35. J. Greulicha *et al.*, *Energy Procedia* **7**, 27 (2012).
36. S. Mack *et al.*, *Photovoltaic Specialists Conf.* (2010).
37. S. Ye *et al.*, *Nano Lett.* **6**, 15 (2015).
38. G. de Cesare *et al.*, *IEEE Electron Device Lett.* **3**, 33 (2012).
39. F. Allen and G. Gobeli, *Phys. Rev.* **1**, 127 (1962).
40. F. Himpsel *et al.*, *Phys. Rev. B* **12**, 28 (1983).
41. H. Rao *et al.*, *ACS Appl. Mater. Interfaces* **12**, 8 (2016).

Funct. Mater. Lett. Downloaded from www.worldscientific.com
by UNIVERSITY OF NEW ENGLAND on 09/21/19. Re-use and distribution is strictly not permitted, except for Open Access articles.